Supplementary Information:

Limitations in Rechargeability of Li-O_2 Batteries and Possible Origins

B. D. McCloskey*, D. S. Bethune, R. M. Shelby, T. Mori, R. Scheffler, A. Speidel, M. Sherwood, and A. C. Luntz*

[1]Almaden Research Center, IBM Research, 650 Harry Rd, San Jose, CA 95120
[2]Central Glass International Inc., 2033 Gateway Pl., Ste. 569, San Jose, CA 95110
[3]Volkswagen Group of America, Inc., Belmont, CA 94002
[4]SUNCAT, SLAC National Accelerator Laboratory, Menlo Park, CA 94025-7015

*bmcclos@us.ibm.com, acluntz@pacbell.net

Experimental details:

All basic experimental procedures have been described in detail in previous studies[1-3] and are only briefly described here. A Biologic VMP3 Workstation is used for all electrochemical characterization.

The DEMS cell has also been described in detail previously. Briefly, Li metal (FMC Corp.), 2 Celgard 2500 separators (wetted by 65 μL electrolyte solution), and a carbon cathode (either XC72-based or P50 carbon paper) are stacked between 2 custom-built electrode tips that allow the battery stack to be hermetically sealed using compressed o-rings against a fused silica tube. The cell is assembled and disassembled in an Argon glove box and special care is taken to ensure that the cell contents are never exposed to ambient atmosphere. Two capillaries are silver soldered into the cathode tip to allow gasses to be dosed into and out of the ~1.5 mL cell headspace. The headspace can be isolated and an in-line pressure transducer can measure pressure decay, from which the total amount of oxygen consumed during discharge can be calculated from the accurately calibrated headspace volume. During charge, the quantitative composition of the headspace gas swept out of the cell is analyzed using a calibrated residual gas analyzer (Stanford Research Systems). In this case, the absolute quantities of the different gas components are determined by comparing the calibrated mass spectrometer intensity for the various masses to the ^{36}Ar peak of known Ar headspace pressure and volume.

XC72 cathodes were prepared by air-spraying an XC72/PTFE slurry onto 316SS 100 mesh (TWP, Inc., Berkeley, CA). The slurries were prepared by sonicating XC72 and PTFE (60 wt% dispersion in water, Sigma Aldrich) in a 5:1 wt:wt ratio in a 20:80 isopropanol:water (IPA:H_2O) mixture. A Badger model 350 air-sprayer was used to uniformly coat the SS mesh (the SS mesh was rinsed in acetone, sonicated in 2M H_2SO_4 for 1h, followed by a multiple water and acetone rinses prior to cathode preparation). Prior to cutting 12 mm diameter cathodes from the carbon-coated SS mesh, the mesh was allowed to air dry for 1h. All cathodes were then washed in pure DME in a glove box, followed by drying first under vacuum for 10 minutes, and

then at 200° C in a glove box for at least 1h. Typical XC72 loading was 1-2 mg. Ballard AvCarb P50 carbon fiber paper (P50) was purchased from the Fuel Cell Store and used after a similar rinsing/drying procedure outlined above. Chemical rechargeability was similar regardless of the type of carbon cathode employed in our previous study[3], and we therefore have used P50 and XC72-based cathodes interchangeably in this study.

Dimethoxyethane (DME), tetrahydrofuran (THF), triglyme (TGE), acetonitrile (CH_3CN), lithium bis(trifluoromethane sulfonyl) imide (LiTFSI), lithium tetrafluoroborate ($LiBF_4$), Lithium triflate (LiTrif), and Lithium bis(oxalato) borate (LiBOB) were purchased from Novolyte and used as received. N-methyl pyrrolidone (NMP) and dimethyl sulfoxide (DMSO) were purchased from Sigma Aldrich and vacuum distilled prior to use. Lithium perchlorate ($LiClO_4$, battery grade, 99.99%) was also purchased from Sigma Aldrich and used as received. N-methyl-N-propylpiperidinium bis(trifluoromethylsulfonyl) imide (MPP-TFSI) was purchased from Wako Chemicals and dehydrated using CaH_2, followed by filtration through a syringe filter. The tri(ethylene glycol)-substituted trimethylsilane (known in the literature as 1NM3) was synthesized by adding trimethylchlorosilane (1.4 equiv.) to a stirred solution of triethylene glycol monomethylether and triethylamine (1.4 equiv.) in an ice bath. The mixture was stirred at room temperature for 2 h, followed by heating to 45 °C for 2 h. After filtration through a layer of celite, the filtrate was concentrated under vacuum. The product was purified by silica gel column chromatography using an acetone-hexane (2:8) mixture as the elution solvent. The final product was obtained by vacuum distillation, bp 86-88 °C at 4 Torr. This solvent was found to be 99.5% pure via GC-MS, with the only detectable contaminant being tri(ethylene glycol) monomethylether. Therefore, in 65 μL of 1NM3, ~1 μmol of tri(ethylene glycol) monomethyl ether is present, which accounts at most for 9% of the total O_2 consumed during the discharge in Figure S1/Table 1. All other solvents used in this study were stored in an Argon glove box (0.1 ppm O_2 and H_2O), had no detectable impurities by ^1H, ^{13}C NMR and GC-MS, and contained <20 ppm H_2O (Karl-Fischer titration).

Two other ionic liquids, 1-ethyl-3-methylimidazolium bis(trifluoromethylsulfonyl imide) and diethylmethyl (2-methoxyethyl)ammonium bis(trifluoromethylsulfonyl imide), evolved significant amounts of H_2 and visibly turned yellow either prior to or during discharge. Thus, these ionic liquids were either not stable to Li metal or Li_2O_2 and were not studied further.

Figures S5, S7-9 ($LiFePO_4$ anode discussion):

Figure S5 compares oxidative potential scans for DME and CH_3CN-based cells similar to those in Figure S4, but with $LiFePO_4$ as the anode. CH_3CN exhibits the higher oxidation potential U_{ox}, in agreement with standard tables of oxidation potentials. Acetonitrile's oxidation potential versus Li/Li^+ can unfortunately not be measured directly since CH_3CN is unstable to Li metal as it does not form a stable SEI. In addition, since the $LiFePO_4/Li^+$ equilibrium potential may vary with solvent

differently than that of Li/Li^+, the comparison of DME's U_{ox} to both references cannot be used to quantitatively scale CH3CN's U_{ox} against $LiFePO_4/Li^+$ to Li/Li^+. Therefore, we simply believe that Figure S5 implies that U_{ox} (CH_3CN) > U_{ox} (DME), both relative to Li/Li^+. It is also apparent in Figure S5 that the electrolyte oxidation currents turn on much more gradually than those in Figure S5 using the Li metal anode. We believe this is due to the slow kinetics of the $LiFePO_4$ anode (see discussion below and Figure S9).

Figure S7 shows that a ~2 e^-/O_2 process occurs at all potentials during reduction for both DME and CH_3CN when employing a $LiFePO_4$ anode. The oxidative scan shows that the electrochemical process is ~2e^-/O_2 to higher potentials in CH_3CN than in DME. Thus, the electrochemical stability of these electrolytes scale approximately with U_{ox}, in agreement with observations made in Figures 1 and 2 in the main article.

Figure S8 compares a galvanostatic discharge-charge cycle in DME using the $LiFePO_4$ anode to that using a Li metal anode. Using the $LiFePO_4$ anode gives somewhat higher discharge and charge overpotentials. This most likely arises from polarization losses at the anode due to the slow de-intercalation and intercalation into $LiFePO_4$. These overpotentials are observed using LiFePO4 as the working electrode in a cyclic voltammogram in a bulk electrolysis cell using Li metal as the counter and reference electrode (Figure S9). When a modest scan rate is used (Figure S9a), no reduction/oxidation peaks are observed in the CV, whereas at very low scan rates (Figure S9b), reduction/oxidation peaks are clearly observed and are centered 3.4V. Figure S8 also shows that although the exact shape of the loss in OER is different for the two anodes (possibly because of the different shapes of overpotentials), the total OER/ORR is the same for both anodes. This certainly argues that all losses in OER are associated with the cathode electrochemistry.

References:

1. McCloskey, B. D.; Bethune, D. S.; Shelby, R. M.; Girishkumar, G. & Luntz, A. C. Solvents' critical role in nonaqueous lithium–oxygen battery electrochemistry. *J. Phys. Chem. Lett.* **2011**, 2, 1161-1166.
2. McCloskey, B. D.; Scheffler, R.; Speidel, A.; Bethune, D. S.; Shelby, R. M. & Luntz, A. C. On the efficacy of electrocatalysis in nonaqueous Li–O_2 batteries. *J. Am. Chem. Soc.* **2011**, 133, 18038-18041.
3. McCloskey, B. D.; Speidel, A.; Scheffler, R.; Miller, D. C.; Viswanathan, V.; Hummelshøj, J. S.; Nørskov, J. K. & Luntz, A. C. Twin problems of interfacial carbonate formation in nonaqueous Li–O_2 batteries. *J. Phys. Chem. Lett.* **2012**, 3, 997-1001.

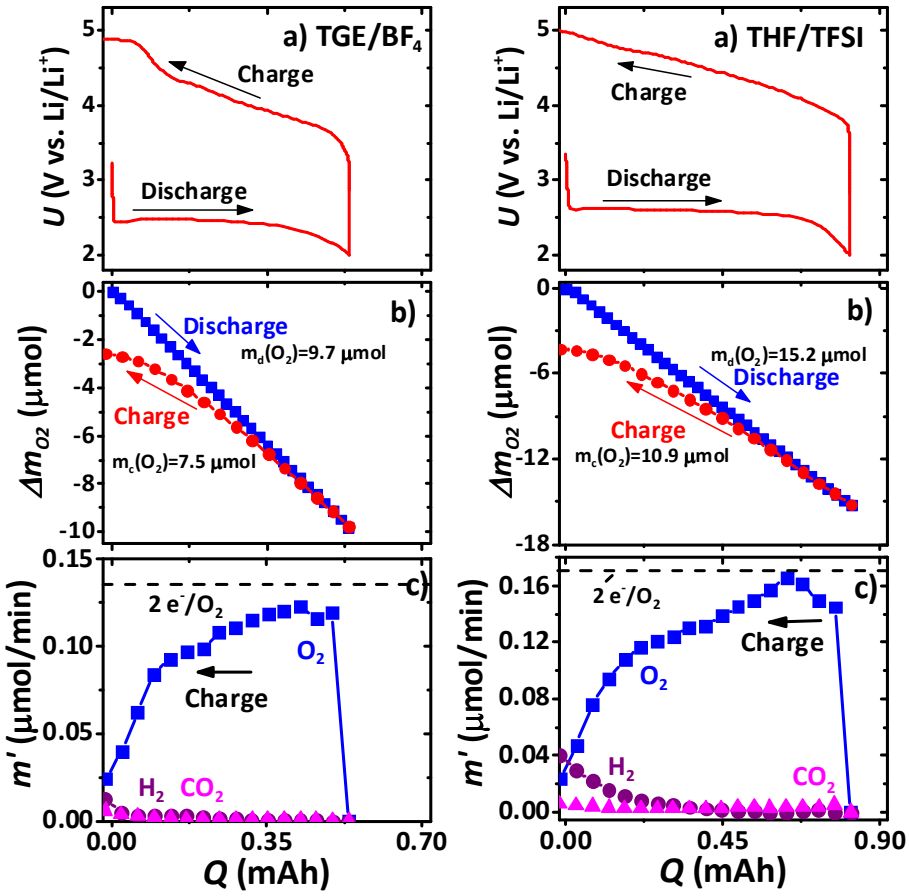

Figure S1: a) Galvanostatic discharge-charge curves for cells employing 1N $LiBF_4$ in triglyme and 1 N LiTFSI in THF. XC72 cathodes were used (350 mA/gcdischarge-charge). b) Oxygen consumption during discharge (measured using pressure decay) and evolution (measured using DEMS) during charge. c) Gas evolution rates for H_2, CO_2, and O_2 (these were the only gases found to evolve during charge) during cell charge.

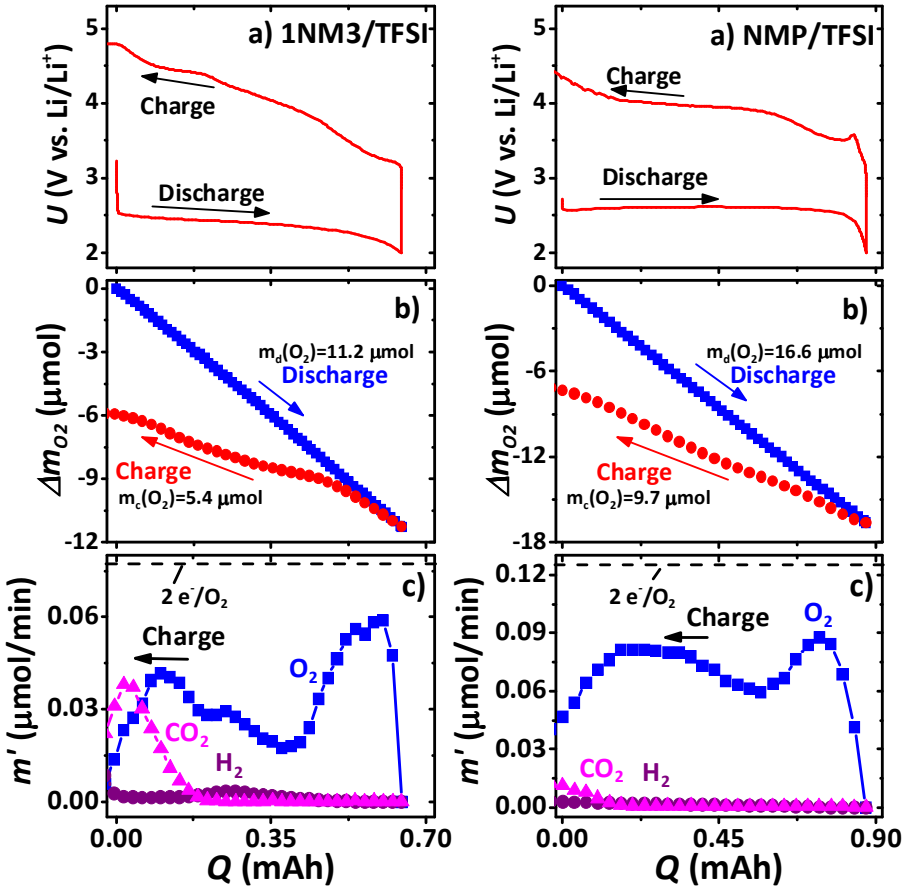

Figure S1 (cont): a) Galvanostatic discharge-charge curves for cells employing 0.3M LiTFSI in MPP-TFSI and 1NM3, respectively. P50 was used as the cathode for the MPP-TFSI/TFSI cell (15 µA discharge-charge), and an XC72-based cathode was used for the 1NM3/TFSI and NMP/TFSI cell (350 mA/gc discharge-charge). b) Oxygen consumption during discharge (measured using pressure decay) and evolution (measured using DEMS) during charge. c) Gas evolution rates for H_2, CO_2, and O_2 (these were the only gases found to evolve during charge) during cell charge.

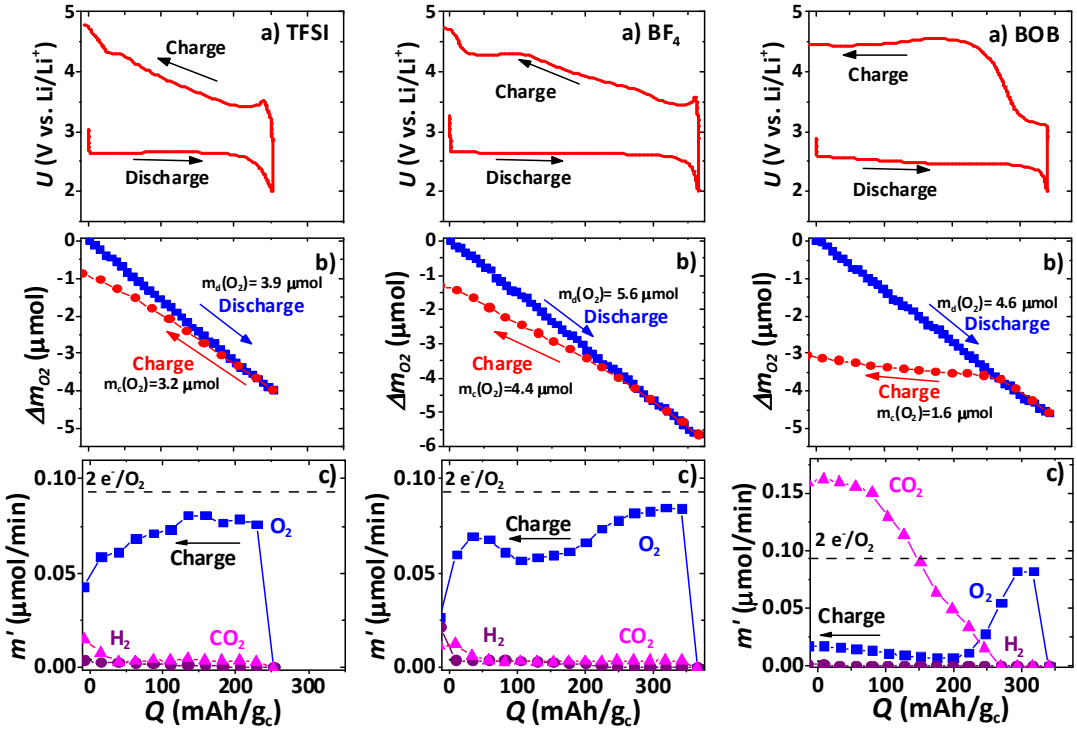

Figure S2: a) Galvanostatic discharge-charge (350 mA/g XC72) curves for DME-based Li-O_2 cells employing LiTFSI, $LiBF_4$, and LiBOB (1M concentration for all salts). b) Oxygen consumption during discharge (measured using pressure decay) and evolution (measured using DEMS) during charge. c) Gas evolution rates for H_2, CO_2, and O_2 (these were the only gases found to evolve during charge) during cell charge.

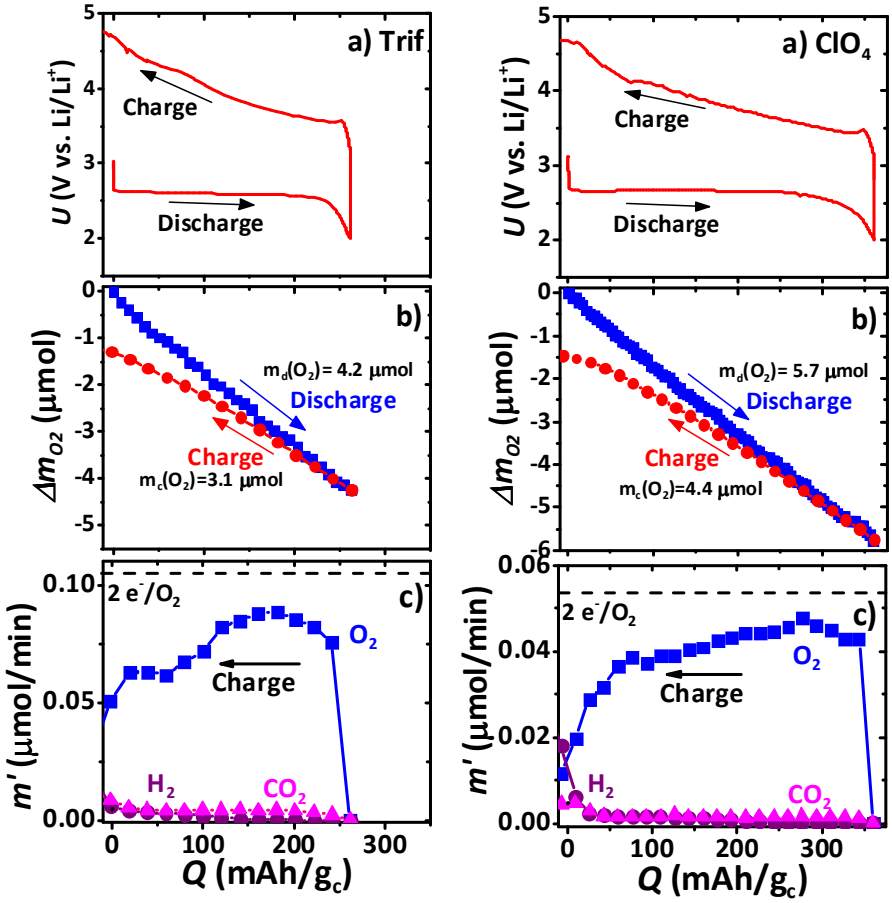

Figure S2 (cont.): a) Galvanostatic discharge-charge (200 mA/g XC72 for $LiClO_4$ and 350 mA/g XC72 for LiTriflate) curves for DME-based Li-O_2 cells employing LiTriflate (1N) and $LiClO_4$ (0.2N). b) Oxygen consumption during discharge (measured using pressure decay) and evolution (measured using DEMS) during charge. c) Gas evolution rates for H_2, CO_2, and O_2 (these were the only gases found to evolve during charge) during cell charge.

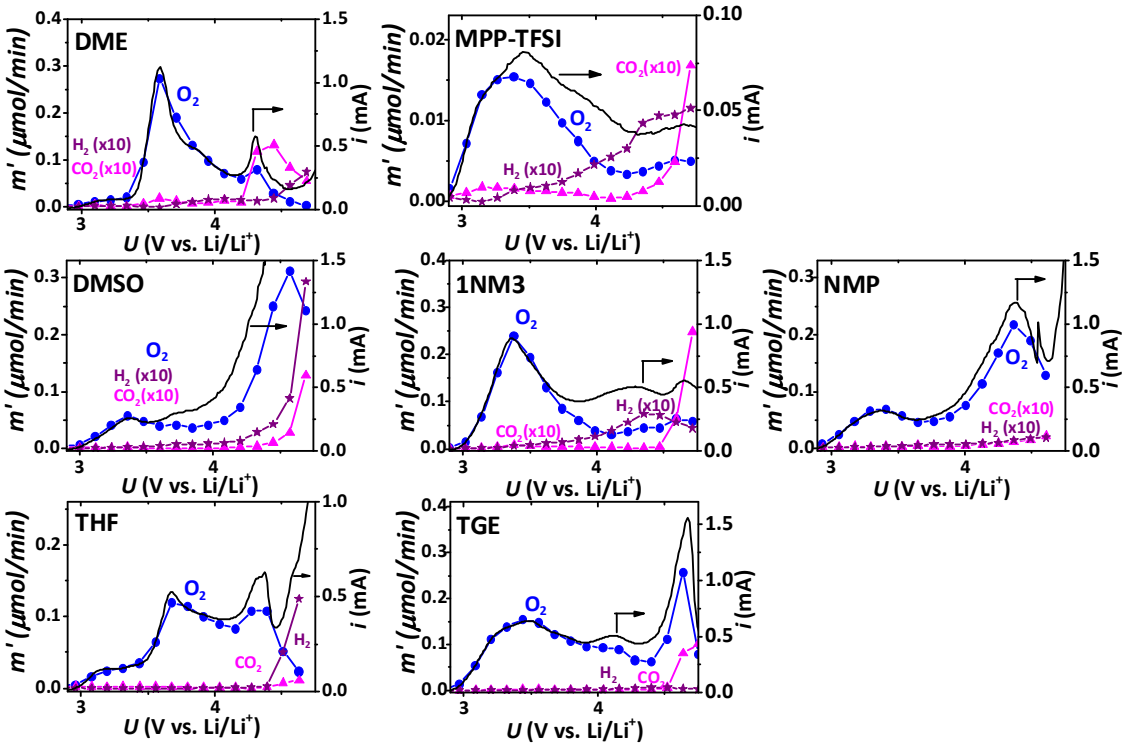

Figure S3: Oxidative potential scans (0.5 mV/s under Ar) for all solvents studied following a 250 mA/g_c discharge under O_2 for 2h or 2V vs. Li/Li^+ (XC72-based cathodes). The ordinate scale ranges were adjusted for each solvent such that m'_{O2} and i overlay at the beginning of the scan. A $2e^-/O_2$ process would correspond to a m'_{O2} [μmol/min]/i [mA] ratio of 0.31.

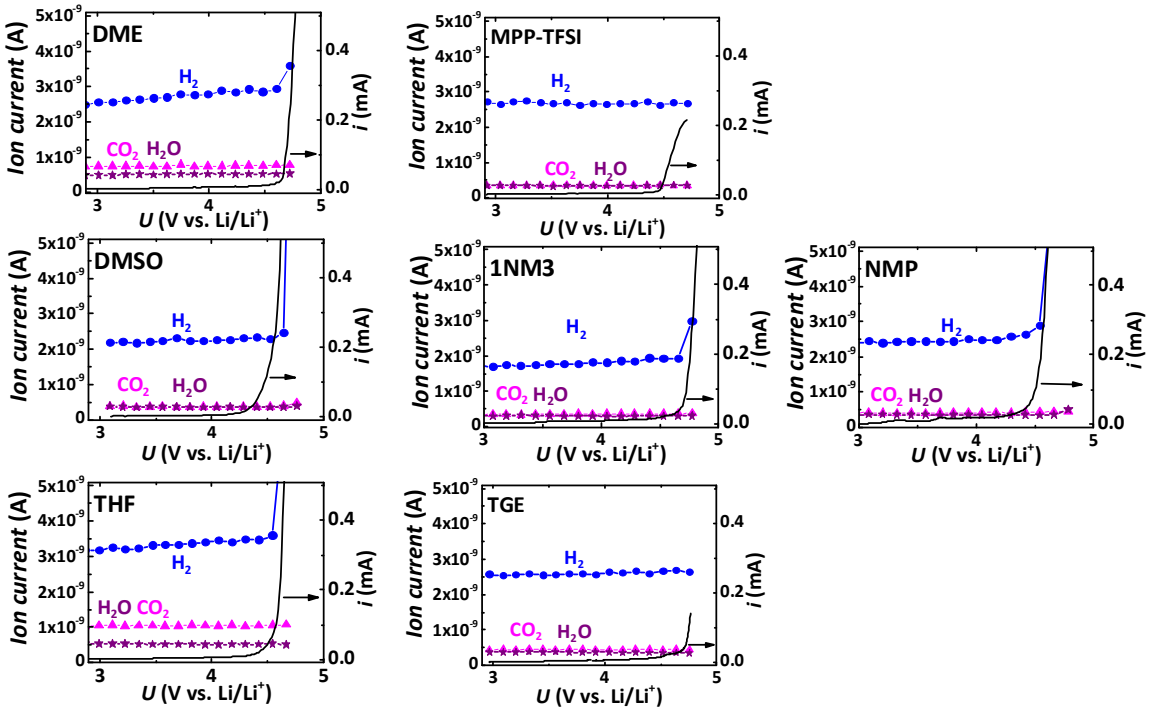

Figure S4: Oxidative potential scans (0.5 mV/s under O_2) for all solvents studied without prior discharge (P50 cathode). Ion current is reported here instead of molar generation rate because these data were acquired under an O_2 headspace, whereas all other data were acquired under an Ar headspace. The Ar headspace allowed us to calibrate all gases evolved by comparing each gas' ion current to the ion current of the ^{36}Ar isotope, whereas a similar calibration was not possible under O_2. However, the molar generation rate of these gases is directly proportional to the difference between the ion current and its baseline value, which was established at the beginning of each voltammetric sweep.

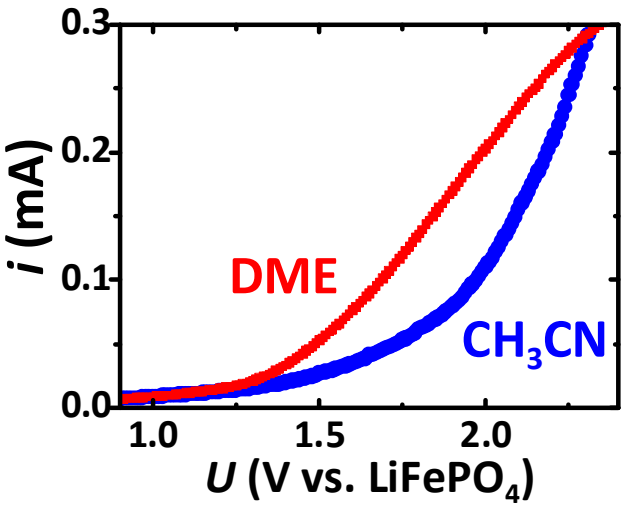

Figure S5: Oxidative potential scans for cells employing a $LiFePO_4$ anode (1N $LiBF_4$ in DME or CH_3CN). Cell properties: P50 cathode, 0.1 mV/s under O_2. No gases were evolved over the potential range shown. The open circuit potential of both cells was slightly less than 0 V vs. $LiFePO_4$; only capacitive current is drawn below the potential range shown.

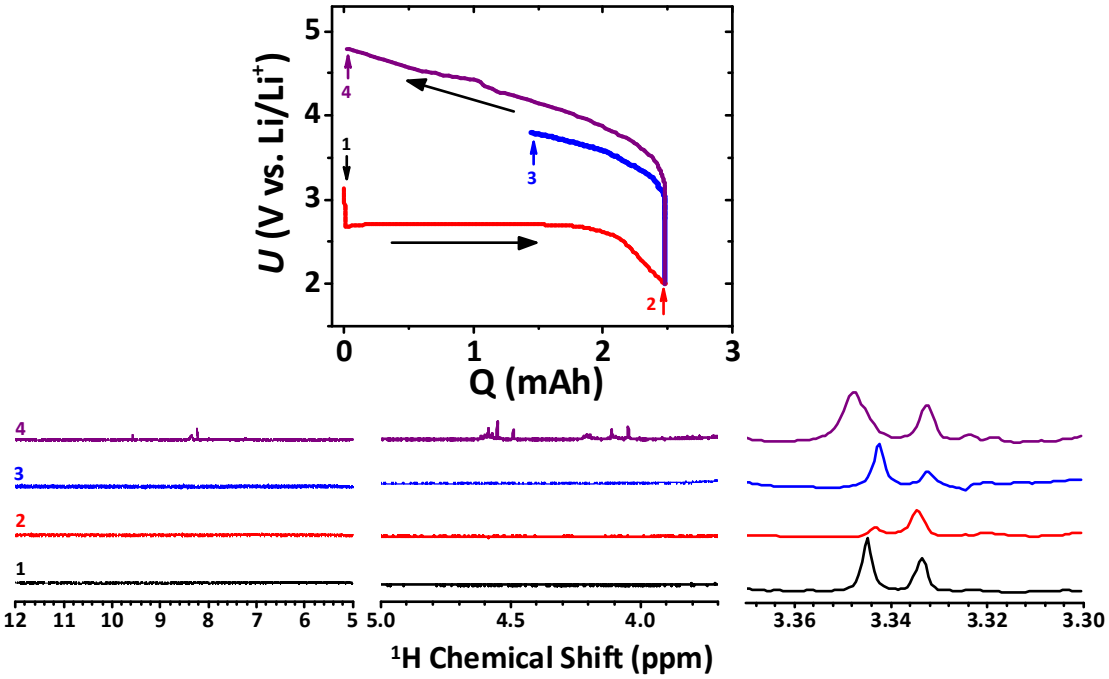

Figure S6: ^{1}H NMR of electrolyte extracted from a 1N TFSI in DME cell at various points during a chronopotentiometric discharge-charge cycle. A ketjenblack-based cathode (~1 mg carbon loading) was employed. A 200 μA discharge was used in each experiment. The charge to 3.8 V (3) was performed at 200 μA under Ar, the fullcharge (4) was performed at 400 μA under Ar. Similar discharge capacities (~2.5 mAh) were observed for all experiments.

Discussion of Figure S6:

65 μL (the total volume of solvent used in the cells studied in Figure S6) of DME corresponds to ~600 μmols DME. A 2 e^- electrochemical process would yield ~45 μmol product during a 2.5 mAh discharge (which is approximately the capacity of the cells used in Figure S6). The detection limit of the ^{1}H NMR is ~$2x10^{-4}$ mol fraction relative to the total DME in the NMR sample, indicating that at most 0.12 μmols of liquid-phase decomposition products were produced during discharge and charge to only 3.8 V. In the full charge NMR (i.e., curve 4), the decomposition products observed in between 4-5 ppm and 7-10 ppm are ~$2x10^{-3}$ mol fraction of total DME, which corresponds to 1.2 μmol of total decomposition products. The peak at ~3.35 ppm is attributed to H_2O, and the peak at 3.33 ppm is attributed to a 2nd order spinning sideband from methyl endgroups in DME. The higher amount of H_2O initially present in the cells relative to the electrolyte content is most likely a result of H_2O desorbed from the Celgard separators and porous carbon cathode, even though both were carefully handled and baked prior to cell assembly.

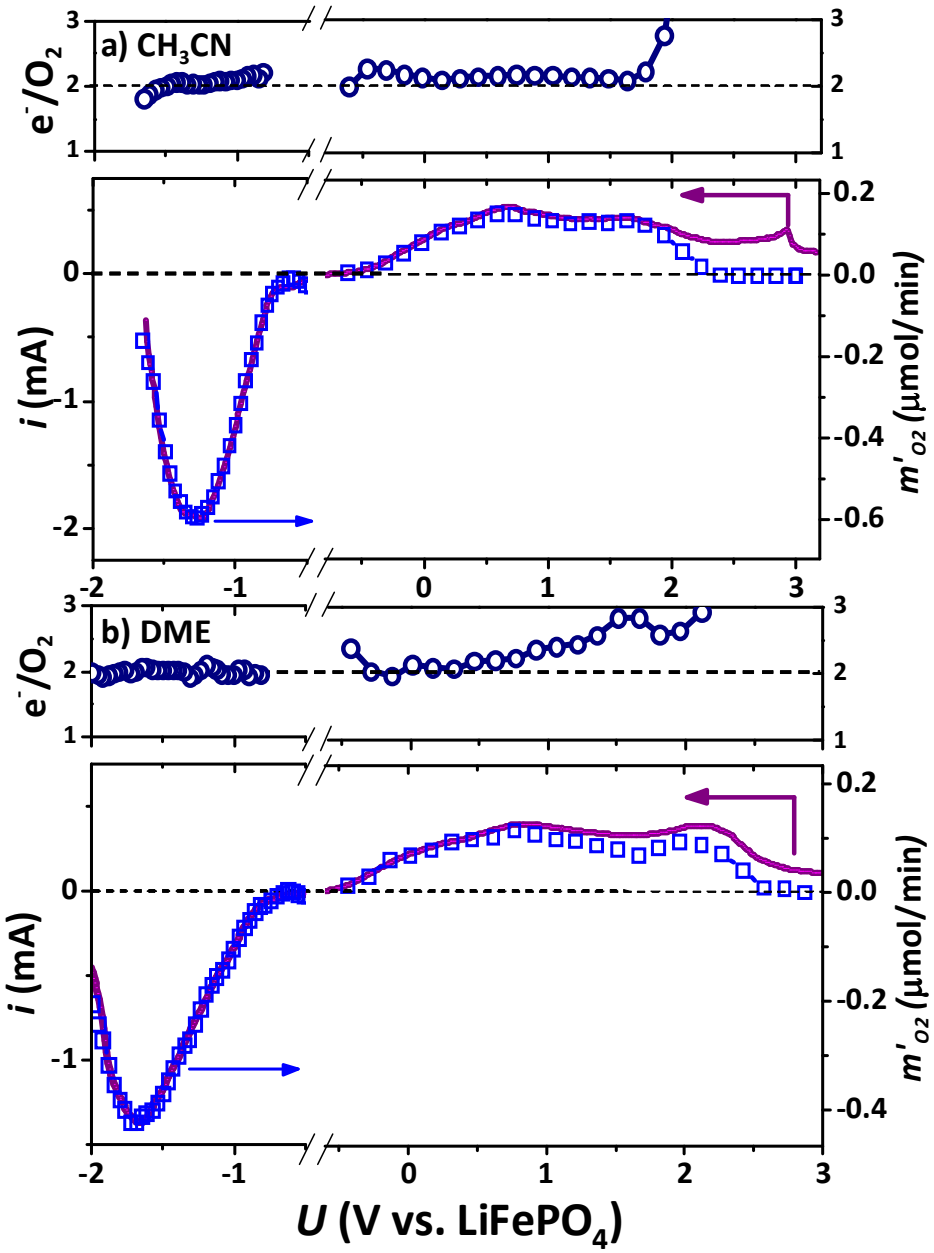

Figure S7: Reductive (under O_2) and oxidative (under Ar) potential scans (0.5 mV/s) for 1N $LiBF_4$ in a) CH_3CN and b) DME. Cell properties: XC72-based cathode, $LiFePO_4$ anode. e^-/O_2 are given for each potential. Pressure decay measurements are used to calculate O_2 consumption during the cathodic scan and DEMS measurements are used to calculate O_2 evolution on the anodic scan.

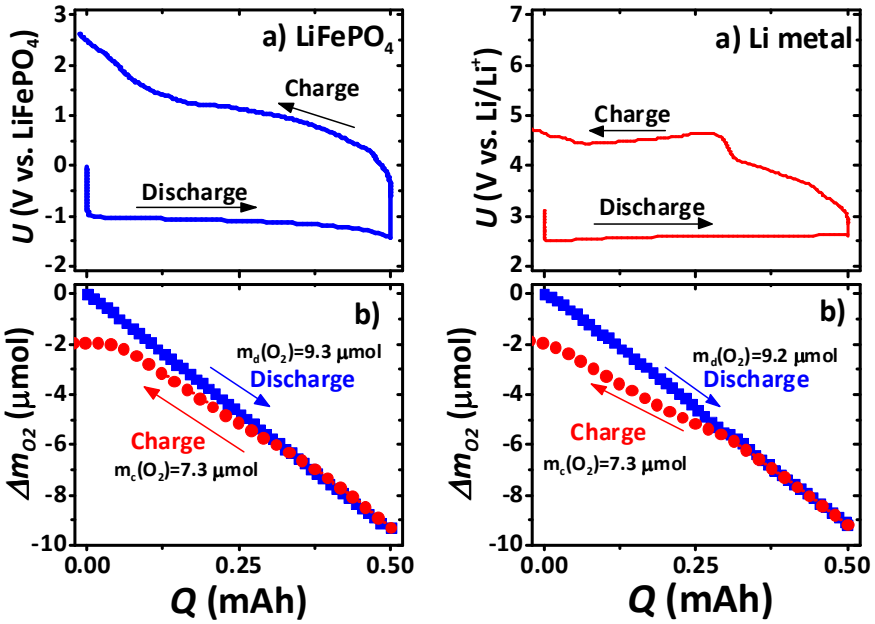

Figure S8: a) Galvanostatic discharge-charge for cells employing a $LiFePO_4$ anode (1N $LiBF_4$ in DME) and a Li metal anode (1N LiTFSI in DME). b) Oxygen consumption during discharge and evolution during charge. Other cell properties: P50 cathode, 500 µA discharge under O_2, 250 µA charge under Ar.

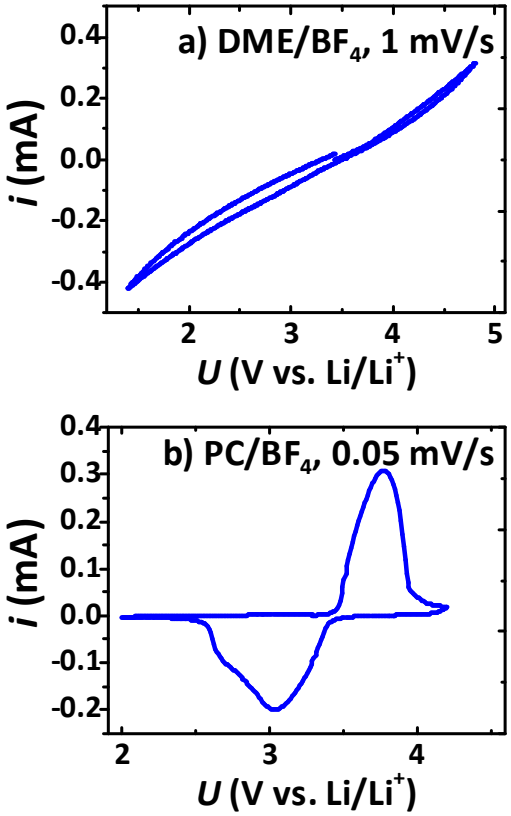

Figure S9: Cyclic voltamograms in a bulk electrolysis cell employing $LiFePO_4$ as the working electrode and a Li metal counter and reference electrode. a) 1N $LiBF_4$ in DME was used as the electrolyte and the scan rate was 1 mV/s, b) 1N $LiBF_4$ in propylene carbonate was used as the electrolyte and the scan rate was 0.05 mV/s. Scans were performed under Ar. The bulk electrolysis cell was similar to that used in previous studies.

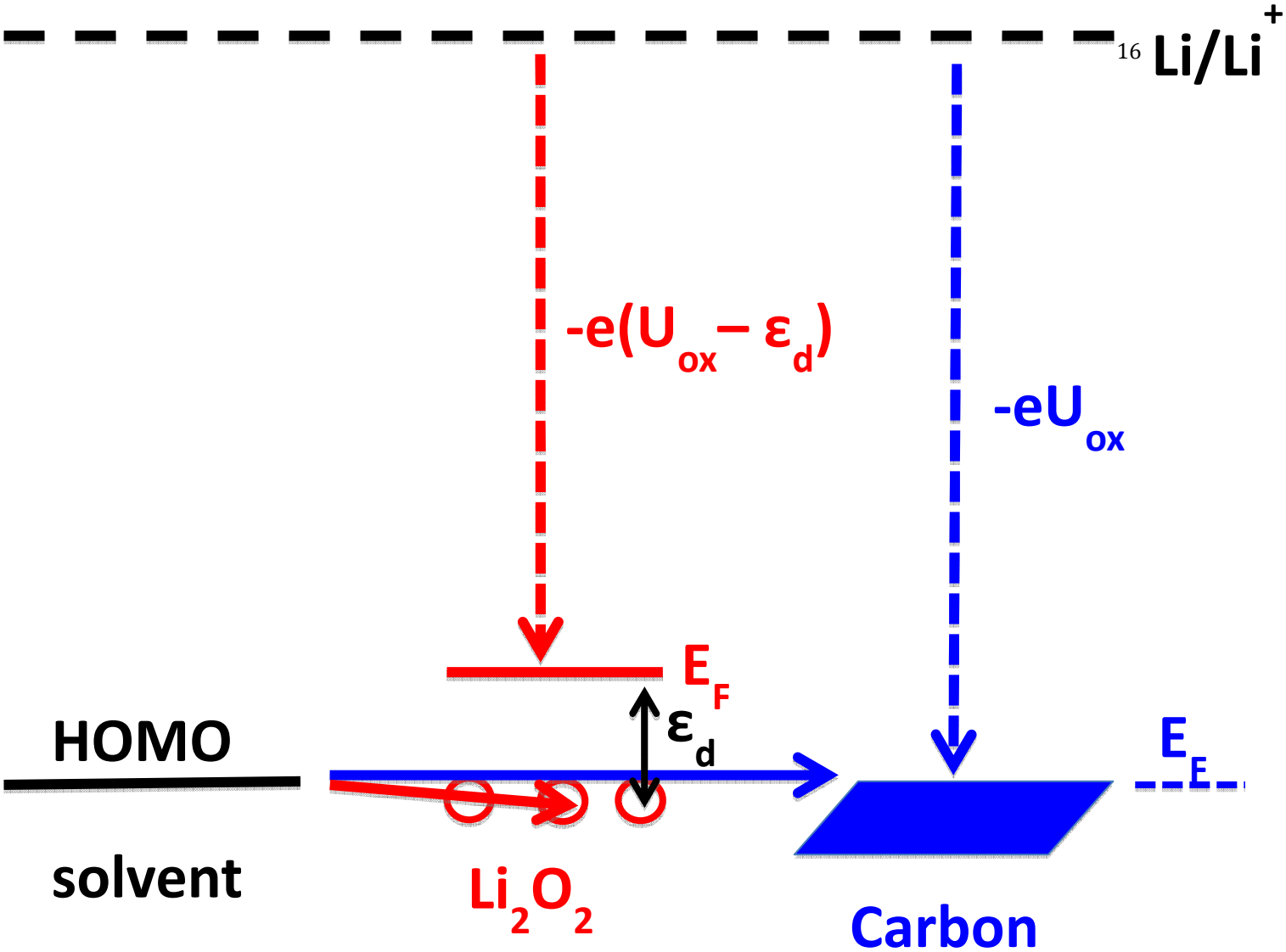

Figure S10. Charged particle free energy diagram for a solvent, a Li_2O_2 electrode and a Carbon electrode at potential U_{ox} relative to Li/Li+ applied to the electrode. The electron free energies are given as lines and hole free energies as circles. The solvent electron free energy is given by the highest occupied molecular orbital (HOMO), while that for the Carbon electrode is defined by the Fermi energy E_F that shifts with the applied potential. The blue arrow shows when electron transfer is possible from the solvent to the C electrode (solvent oxidation at U_{ox}). For a Li_2O_2 electrode, the circles represent unoccupied positively charged defects representing hole energies at ε_d below E_F. If plotted as electron energies, they would appear at ε_d above E_F. since hole energies are the negative of electron energies. Therefore, solvent oxidation may occur at potential U_{ox} - ε_d/e.